A study of large plastic deformations in dual phase steel using digital image correlation and FE analysis

Venkat Tarigopula, Odd Sture Hopperstad, Magnus Langseth, Arild H. Clausen, François Hild, Odd-Geir Lademo, Magnus Eriksson

A study of large plastic deformations in dual phase steel using digital image correlation and FE analysis

V. Tarigopula[*1], O. S. Hopperstad[1], M. Langseth[1], A. H. Clausen[1], F. Hild[2], O.-G. Lademo[3, 1] and M. Eriksson[3]

[1]*Structural Impact Laboratory (SIMLab),*
Centre for Research-based Innovation (CRI),
Department of Structural Engineering,
Norwegian University of Science and Technology,
NO-7491 Trondheim, Norway
[2]*Laboratoire de Mécanique et Technologie (LMT-Cachan),*
Ecole Normale Supérieure de Cachan / CNRS-UMR 8535 / Université Paris 6,
61 Avenue du Président Wilson, F-94235 Cachan Cedex, France
[3]*SINTEF Materials and Chemistry,*
NO-7465 Trondheim, Norway

Abstract

Large plastic deformation in sheets made of dual phase steel DP800 is studied experimentally and numerically. Shear testing is applied to obtain large plastic strains in sheet metals without strain localisation. In the experiments, full-field displacement measurements are carried out by means of digital image correlation, and based on these measurements the strain field of the deformed specimen is calculated. In the numerical analyses, an elastoplastic constitutive model with isotropic hardening and the Cockcroft-Latham fracture criterion is adopted to predict the observed behaviour. The strain hardening

[*]Corresponding author. Tel.: + 47 73 59 46 90; fax: + 47 73 59 47 01.

E-mail address: venkatapathi.tarigopula@ntnu.no (V. Tarigopula).

parameters are obtained from a standard uniaxial tensile test for small and moderate strains, while the shear test is used to determine the strain hardening for large strains and to calibrate the fracture criterion. Finite Element (FE) calculations with shell and brick elements are performed using the non-linear FE code LS-DYNA. The local strains in the shear zone and the nominal shear stress-elongation characteristics obtained by experiments and FE simulations are compared, and, in general, good agreement is obtained. It is demonstrated how the strain hardening at large strains and the Cockcroft-Latham fracture criterion can be calibrated from the in-plane shear test with the aid of non-linear FE analyses.

Keywords: shear test, DP800, sheet metal, digital image correlation, numerical simulations, ductile fracture, Cockcroft-Latham fracture criterion.

1 Introduction

In the recent years, high strength steels are increasingly used in lightweight applications such as closure and structural panels in the automotive industry in a quest for lighter and safer vehicles. Such applications typically call for sheet metal forming processes including stamping, stretch flanging and deep drawing. These forming processes lead to large plastic deformations of the sheets and severe strain path changes while transforming them into structures. Fracture in vehicle parts may occur as a result of the forming processes during car crashes, where it may be detrimental for the energy dissipation capability of the structure. In view of the above facts, fundamental understanding and tools for the

prediction of material behaviour at large deformations including failure are indispensable for improving the performance of automotive structures.

Uniaxial tensile tests are the most widely used experiment for determining the elastoplastic behaviour of materials. However, in this test ductile fracture usually occurs after diffuse and localised necking, and accurate measurements of large plastic deformations up to fracture are hampered by these plastic instability modes [1]. Hence, alternative material tests are needed to characterize the behaviour of sheet metals for large plastic strains and complex loading paths. Among the possible choices, the shear test is particularly attractive for sheet materials since large strains are achieved without the occurrence of plastic instabilities [2-4].

Numerous experimental and numerical studies have shown that the shear test, ranging from simple shear to pure shear, is a very efficient technique for evaluating the material properties of sheet specimens under complex loadings or strain path changes [1-9]. In simple shear one direction remains constant and everything else rotates relatives to it, while directions of greatest compression and extension are constant in pure shear. Iosipescu [7] designed a new procedure for pure shear testing using notched specimens subjected to antimetric four-point bending. This test is particularly attractive for the in-plane shear testing of composites. The advantage of this method is the use of small specimens without the need of grips to hold the specimen during testing, and the existence of a uniform shear region between the notches. However, non-uniform stress distributions might occur around the roots of the notches depending on the specimen orthotropy ratio [8] or damage state

[10], and this may further introduce difficulties in evaluating ductile damage and fracture. On the other hand, simple shear tests were performed by some researchers [2-6] using a planar simple shear apparatus. The specimens are very easy to prepare and have a simple rectangular shape. This technique has been adopted for studying the flow localisation induced by a change in strain path [5], and plastic anisotropy of sheet metals at large strains [2-4]. However, care should be taken to obtain proper gripping of the specimen during deformation, since it critically influences the response of the specimen. In particular, premature failure inside the grips should be avoided because of the heterogeneous stress distribution at corners [4].

Bao and Wierzbicki [9] presented a novel shear test specimen with a butterfly gauge section and reduced thickness in the shear zone. This specimen is designed to be used for characterizing fracture for low stress triaxiality conditions. The reduced thickness in the shear zone requires machining of the material that may introduce surface effects such as residual stresses and microcracks. Moreover, the plastic deformation of the machined shear zone may result in a non-planar stress state that could make the results difficult to interpret when evaluating planar anisotropic materials, and in particular when thin shell approximations are used in the numerical simulations. Lademo et al. [1] proposed a modified specimen design based on Bao and Wierzbicki's [9] geometry without the reduced thickness in the shear zone, but that retains the predominant pure shear in the confined zone and ensures fracture initiation within the gauge area rather than at the free edge. The shear test may in addition to fracture strain investigations also be used to identify hardening parameters in a range of effective plastic strains and for combination of stresses

that are not explored by standard uniaxial tension tests. However, the shear specimen has a complex shape with a confined shear zone. The complex shape makes it difficult to obtain accurate measurements of the development of strains within the shear zone. Therefore, it is worth considering full-field measurements over the shear zone in order to obtain estimates of local displacements and strains. These measurements are helpful in further improvements of the specimen design and in interpretation of test results. In the literature, various full-field measurement techniques have been used for displacement and strain field measurements based on digital images. Of particular interest is the relatively simple, computationally inexpensive and robust algorithm based on digital image correlation (DIC) [11-13].

The objective of the present work is twofold. First, the local strains in the shear zone of the specimen will be determined by using digital image correlation (DIC). Thereafter, these measurements will be compared with results from a series of numerical simulations using the non-linear explicit solver of the FE code LS-DYNA. The second objective is to demonstrate the use of the shear test to determine the strain hardening at large strains and to calibrate the Cockcroft-Latham fracture criterion. This requires good agreement between the experimentally and numerically obtained strain fields in the shear zone and nominal shear stress vs. elongation characteristics.

2 Experiments

2.1 Material

The dual-phase high-strength steel DP800 (chemical composition in wt % – C: 0.12, Si: 0.20, Mn: 1.50, P: 0.015, S: 0.002, Nb: 0.015, Fe: bal.), which consists of a mixture of 70 % ferrite and 30 % martensite (vol. %), was considered in the present investigation. The steel was supplied by Swedish Steel Works, SSAB. In the as-received state, the ferrite grains are nearly equiaxial with a size of 5-10 μm, while the martensite phases, usually present at the grain boundaries, have a size in the order of 2-5μm. This steel possesses the combined attributes of excellent formability (ductility) and high strength, which allow for the use of thinner sheets in industrial applications. Accordingly, the specimens in this study were taken from a cold-rolled sheet of nominal thickness 1.5 mm. The thickness variation along the sheet was found to be less than 2 %. The material was characterized by using monotonic quasi-static tensile tests and in-plane shear tests in the as-received state. The tensile tests were performed in different orientations from the rolling direction in order to assess potential plastic anisotropy of the material.

2.2 Tensile tests

Uniaxial tensile tests were carried out at room temperature by using a conventional servo-hydraulic Dartec testing machine with a load capacity of 20 kN. Tensile specimens in accordance with the ASTM standard, 1.5 mm thick and with a 5 mm wide gauge section (see Fig. 1), were cut along the rolling direction (0^o), 45^o to the rolling direction and in the transverse in-plane direction (90^o). The gauge length of the specimen was 30 mm. Three duplicate samples in each direction were machined and tested. The specimens, as shown in Fig. 1, were gripped at either end by a suitable fixture in the testing machine and stretched

to fracture under displacement control at a constant cross-head speed of 1.8 mm / min to produce a strain-rate of the order of 10^{-3} /s. Load-deformation curves were obtained using an extensometer over the gauge length, from which the Cauchy stress vs. logarithmic strain curves and the strain-hardening parameters were calculated. For the measurement of plastic strain ratios (R -values), the longitudinal and transverse strains were measured continuously with the aid of an MTS 634.31F-25 one sided extensometer, having a 20 mm gauge length, and an MTS 632.19F-20 transverse averaging extensometer, respectively. Thereafter, the standard equations of plasticity were used to calculate the logarithmic plastic strains from the extensometer readings. The R -values are then determined from

$$R_\alpha = \frac{\varepsilon_w^p}{\varepsilon_t^p} = -\frac{\varepsilon_w^p}{\varepsilon_l^p + \varepsilon_w^p} \tag{1}$$

where α denotes the orientation to the rolling direction, while ε_l^p and ε_w^p refer to the longitudinal and transverse logarithmic plastic strains of the gauge section, respectively. The logarithmic plastic thickness strain, ε_t^p, is calculated by assuming plastic incompressibility. Data were logged with a frequency of 10 Hz.

2.3 In-plane shear tests

2.3.1 Specimen design

Although shear tests have been used quite extensively, there exists no standard geometry. The specimen geometry in the current study was developed for determining the plastic behaviour of sheet metals by Lademo et al. [1] based on the design proposed by Bao and Wierzbicki [9] for low stress triaxiality fracture tests. Numerous specimen geometries were evaluated, experimentally and numerically through FE-based optimisation [1]. Efforts were

made to design the specimen geometry to obtain predominant shear deformation under plane stress conditions, and to avoid plastic instability phenomena. Fig. 2 shows the geometry of the final specimen that has a small and concentrated shear zone of length 2.5 mm. Large parts of the specimen length are used for supporting the shear zone and for the clamping.

2.3.2 Experimental procedure

Two shear specimens were machined such that the *x*-axis coincided with the rolling direction, i.e. the 0^o direction. The specimens were mounted using a clevis and clevis pin at each end, and tested in a standard Dartec hydraulic testing machine with a 20 kN load cell under constant displacement rate of 0.3 mm / min. An MTS 634.31F-25 extensometer with a 30 mm gauge length was attached to the specimen to measure the elongation across the shear zone in the *x*-direction. During testing, the crosshead displacement and the loading force were also measured. Data were recorded at a frequency of 10 Hz using Instron multi-axis software (MAX).

During the shear test, there is no possibility to follow the shear strain evolution directly in the shear zone. Thus, a digital video camera system was employed to obtain optical recordings of the specimen deformation at regular intervals to investigate the local strains in the shear zone. Since these tests were conducted at quasi-static rates, a low-speed camera was sufficient to capture the whole deformation process. The utilized camera was an EHDcmos 1.3 mega pixel digital camera, which acquired the images at a frame rate of 1 frame / sec with a resolution of 256 × 512 pixels (8-bit dynamic range). It should be noted that an increase of frame rate will in general reduce the resolution. Thus, the selected

frame-rate and resolution constitute a compromise. Typically, 440-480 images were captured for each test at quasi-static speeds. Before each test, a random pattern was applied to the surface of the object. This pattern was applied by first coating the surface with black paint and then spraying a white spray paint to the black surface to create speckles. The resulting surface texture is useful for determining displacement and strain fields through digital image correlation. The experimental set-up for these tests is shown in Fig. 3.

3 Digital Image Correlation (DIC)

3.1 Displacement and strain measurements

Digital image correlation is a non-contact optical method to measure displacement and strain fields of a planar object (when only one camera is used) by comparing the random pattern of grey levels of the sample surface during deformation with an initial (reference) image taken prior to loading. In order to obtain in-plane displacement quantities, this method usually employs an image-matching algorithm based upon cross-correlation function [11, 14] to compare a pair of digital images captured before and after a small deformation.

Besnard et al. [15] introduced a finite element framework into the digital image correlation procedure in order to be in direct correspondence with FE simulations while measuring the displacement fields. The region of interest (ROI) of the sample surface is discretized into continuous finite elements (Q4-elements) (see Fig. 4). Each element with four nodes is referred to as a zone of interest (ZOI) and bilinear shape functions are adopted to represent the displacements in each element. Nodal displacements are obtained by optimising the

mean quadratic difference between the grey levels of all the elements in the reference image and the corresponding elements in the deformed image. With the determined displacement field, it is possible to calculate the associated strain field.

The principle of digital image correlation is to match zones from one image to the other by characterizing the similarity between the intensity patterns (Fig. 5), and then to find a local displacement. Initial guesses for nodal displacements are obtained by using a coarse graining technique [13]. Finite element kinematics is a novel technique to regularize the sought displacement field by decomposing the trial displacement field onto a basis of a linear combination of continuous shape functions as proposed in finite element methods. Among the possible choices, the first order shape functions are particularly attractive because of their simplicity. A number of iterations are needed before the required convergence is attained. If necessary, the obtained subpixel displacements can be corrected by using the shift / modulation properties of Fourier transforms. However, all the elements are correlated at one time in this finite element based DIC because of the inter-element connectivity. An in-depth description of the adopted approach has been provided by Besnard et al. [15].

The out-of-plane displacement has a certain influence on the recorded sample surface during deformation, and thereby it influences the in-plane displacement measurements [16]. In this study, as shown in Fig. 3, the lens of the camera is positioned at the same vertical position as the specimen and is placed at a distance of 300 mm from the sample surface.

The effect of the out-of-plane displacement on the in-plane deformations of the ROI is assumed to be negligible.

In this study, different strain measures are used for the shear tests, which all accounts for large deformations and rotations. The choice of strain measures was partly dictated by those available in the FE code LS-DYNA, since it was considered important to compare the local strains obtained by full-field displacement measurements and FE simulations. A Cartesian coordinate system is introduced with the orthogonal base vectors $\mathbf{e}_1$, $\mathbf{e}_2$ and $\mathbf{e}_3$ parallel to the rolling (*x*-), transverse (*y*-) and thickness (*z*-) directions, respectively. The Green-Lagrange strain tensor $\mathbf{E}$ is computed from the deformation gradient $\mathbf{F}$ as

$$\mathbf{E} = \frac{1}{2}(\mathbf{F}^T \cdot \mathbf{F} - \mathbf{I}); \quad \mathbf{F} = \mathbf{R} \cdot \mathbf{U}, \tag{2}$$

where $\mathbf{U}$ is the right stretch tensor and $\mathbf{R}$ is the rotation tensor. The in-plane components E_{11}, E_{22} and E_{12} of the Green-Lagrange strain tensor are calculated from the measured displacement field. Shear deformation may also be characterized by the angle change between two adjacent, orthogonal fibers [17], see Fig. 6 . Consider two adjacent fibres of unit length that are aligned with the base vectors $\mathbf{e}_1$ and $\mathbf{e}_2$ in the initial configuration Ω_0. Assume that the fibres are subjected to a homogeneous deformation field. In the current configuration Ω, the direction of the fibres are then given by the vectors $\mathbf{g}_1 = \mathbf{F} \cdot \mathbf{e}_1$ and $\mathbf{g}_2 = \mathbf{F} \cdot \mathbf{e}_2$, while the angle between them, θ, is obtained as

$$\cos\theta = \frac{\mathbf{g}_1 \cdot \mathbf{g}_2}{|\mathbf{g}_1||\mathbf{g}_2|} = \frac{\mathbf{e}_1 \cdot \mathbf{F}^T \cdot \mathbf{F} \cdot \mathbf{e}_2}{|\mathbf{F} \cdot \mathbf{e}_1||\mathbf{F} \cdot \mathbf{e}_2|} \tag{3}$$

The shear angle γ is then defined by $\gamma = \pi/2 - \theta$. Further, the stretch ratios in the fibre directions are given as $\lambda_1 = |\mathbf{g}_1|$ and $\lambda_2 = |\mathbf{g}_2|$, since the length of the fibres in the initial configuration was unity. The thinning of the sheet is defined by the logarithmic thickness strain ε_{33}. To calculate ε_{33}, it is assumed that elastic strains are negligible and that plastic incompressibility prevails. Plastic incompressibility implies that $\det \mathbf{F} = 1$. Further, the components F_{13}, F_{31}, F_{23} and F_{32} of the deformation gradient are all assumed to vanish for the actual deformation fields. With these assumptions, the logarithmic thickness strain may be calculated as $\varepsilon_{33} = \ln F_{33} = -\ln(F_{11}F_{22} - F_{12}F_{21})$. It is also worth noting that the stretch ratio in the thickness direction is $\lambda_3 = \exp \varepsilon_{33}$, which could be used as an alternative measure for the thinning of the sheet. However, in predominant shear deformation the thinning is expected to be relatively small, and the difference between the two measures of less importance.

3.2 Measurement uncertainties

The performance of the digital image algorithm is evaluated a priori in terms of displacement uncertainty. To obtain an estimate of the uncertainty associated with the correlation algorithm, an artificial image is constructed from the recorded picture of one representative test by applying artificially known displacements ranging from 0 to 1 pixel with 0.1 pixel increments using the shift/modulation property of the Fourier transform. Thereafter, the correlation algorithm is applied to this pair of images, thus allowing an evaluation of the uncertainty. In this way, the a priori performance of the algorithm is predicted with an actual picture. The quality of the estimate is characterized by the standard uncertainty, σ_u, which is defined as the mean of the standard displacement uncertainties.

An indication of the accuracy of this technique is seen in Fig. 7, where the effect of the element (or ZOI) size l on the displacement uncertainty was studied for a representative shear test. A rapid decrease of the uncertainty, σ_u, is observed with the element size l (in pixels), as $\sigma_u \approx A^{\alpha+1} l^{-\alpha}$ with $\alpha \approx 1.35$ and $A \approx 0.8$ pixel. Even though the displacement uncertainty is the lowest for large element sizes, the large displacements prompt us to use small sizes. This means that the displacement uncertainty and the corresponding spatial resolution are the result of a compromise. Thus, for an element size of l = 8 pixels as used for the shear specimen, a displacement uncertainty of the order of 0.04 pixel and a standard strain uncertainty σ_ε of the order of $\sqrt{2}\sigma_u / 2\ell \approx 3.5 \times 10^{-3}$ are obtained. This last result is obtained when the nodal strains are determined by a centred finite difference algorithm [18].

4 Experimental results

4.1 Tensile tests

Three duplicate tests were included in the study for each direction (i.e., 0^o, 45^o and 90^o), and the tests were designated as "mtsxxyy", where mts indicates the tensile specimen, xx represents the orientation to the rolling direction and yy refers to the sample number. Tpical mechanical properties of DP800 obtained by means of the uniaxial tension tests are presented in Table 1. The average static proof stress at 0.2 % permanent plastic strain was found to be approximately 535 MPa and the ultimate strength was about 800 MPa. Engineering stress-strain curves describing the work hardening behaviour for one representative test in each orientation are shown in Fig. 8a. All the curves exhibit a smooth

transition from the elastic to the plastic domain regardless of specimen orientation to the rolling direction.

Fig. 8b shows the logarithmic plastic thickness strain ε_t^p against logarithmic plastic width strain ε_w^p for one representative test in each orientation, and demonstrates the determination of the R-values by linear regression in the uniform plastic deformation region, i.e. from initial yielding to diffuse necking. In Fig. 8b, the solid symbols represent the experimental observations, while the dashed lines indicate the best fits to the experimental data. The slopes of the fitted lines represent the R-values (0.80 to 1.05) that are given in Table 1. The strength and plastic flow anisotropy is seen to be minor and it was therefore decided to neglect plastic anisotropy in the elastoplastic constitutive model established for DP800.

4.2 In-plane shear tests

Two duplicate shear tests were performed in the rolling direction (i.e. 0^o direction), using the specimen design shown in Fig. 2. The tests were specified as "msszz", where mss denotes shear specimen and zz indicates the sample number. The test results in terms of nominal shear stress-elongation characteristics are presented in Fig. 9. The nominal shear stress is the applied force divided by the nominal cross-sectional area of the shear zone. There is no significant scatter observed between the two duplicate tests. The increase of the nominal shear stress is gradual, and the curves do not exhibit any drop in flow stress. Furthermore, the nominal shear stress-elongation curves show no signs of plastic instability (i.e., softening behaviour) taking place before the onset of failure occurs at maximum force.

In order to determine the displacement and strain fields in the shear zone, digital image correlation was employed by means of pictures taken with the digital video camera system. A selected sequence of the deformation for shear specimen, mss02, obtained from the digital video camera is shown in Fig. 10. Note that the frames in Fig. 10 only show a small region of the centre part of the specimen that measures around 8 mm × 12 mm. As can be seen, the deformation started with predominant shear (t_2), and the shearing proceeds ($t_3 - t_5$) involving the formation of a well-defined band. Within the shear zone of the specimen, the deformation, and thus the damage accumulation, becomes highly localised and within this localised zone the fracture initiates. Prior to ductile failure, no significant area reduction was noticed in the shear zone.

The evolution of the digital images at various stages of deformation provides direct information about the local strain distribution. A total of 21 images were chosen randomly for the displacement evaluation in the digital image correlation. Images were selected at large intervals in the beginning and then more images were used during the large deformation stages.

Fig. 11a depicts the shear deformation of a single element taken at the middle of the shear zone in terms of the shear angle γ versus time. It is seen that the shear angle is about 50^o when failure occurs. Fig. 11b shows the logarithmic thickness strain ε_{33} versus time for an element at the centre of the specimen gauge section. There is significant scatter between the duplicate tests, but a maximum thickness strain of about 6 % is estimated at fracture. Note that thinning is not constant over the shear zone and this value might vary depending on the

chosen area of interest. Nevertheless, the shear strains in the shear zone seem to be an order of magnitude larger than the thickness strains.

5 Constitutive model and parameter identification

5.1 Constitutive model

A phenomenological constitutive model for DP800 is presented in this section. Since the material exhibits only weak anisotropic behaviour (see Fig. 8), it was chosen to simulate the in-plane shear tests with an isotropic elastoplastic model. The strains and rotations in the shear test are finite, thus, large deformations are considered in the constitutive model. The main ingredients of the elastoplastic constitutive model are an isotropic yield criterion, a non-linear isotropic hardening rule and the associated flow rule [19]. In addition, the concept of non-local plastic thinning for plane stress analysis [20] and a ductile fracture criterion [21] are used respectively to reduce the mesh dependence of strain localisation and to predict ductile failure. This model is a standard material model (*MAT_135) for use with co-rotational shell elements in LS-DYNA [22]. Applying brick elements instead of shell elements, this model has been implemented in LS-DYNA as a user-defined model [23].

The basic constitutive equations for shell (co-rotational) and brick element formulation are compiled in Table 2. A superposed hat (^) denotes the co-rotational formulation and a superposed dot specifies material time differentiation. It is seen that the co-rotational stress tensor $\hat{\boldsymbol{\sigma}}$ and the co-rotational rate-of-deformation tensor $\hat{\mathbf{D}}$ are adopted as energy conjugate measures of stress and strain-rate for plane-stress formulation. For brick

elements, the Cauchy stress $\boldsymbol{\sigma}$ and the rate-of-deformation tensor $\mathbf{D}$ are taken as energy conjugate measures, using the objective Jaumann stress rate $\boldsymbol{\sigma}^{\nabla J}$ in the hypoelastic relation.

The linear hypoelastic relation, which defines the objective stress rate $\boldsymbol{\sigma}^{\nabla J}$ (or $\hat{\dot{\boldsymbol{\sigma}}}$) in terms of the elastic rate-of-deformation $\mathbf{D}^e$ (or $\hat{\mathbf{D}}^e$), is assumed to be isotropic, i.e. $\mathbf{C}$ is an isotropic 4th order tensor, which is determined by Young's modulus E and Poisson's ratio υ. The generalized associated flow rule is adopted to establish the plastic rate-of-deformation tensor $\mathbf{D}^p$ (or $\hat{\mathbf{D}}^p$) and the effective plastic strain rate $\dot{\bar{\varepsilon}}$. The consistency condition, $\dot{f} = 0$, is utilized to determine the plastic multiplier $\dot{\lambda}$ during a plastic process.

The yield criterion $f = \bar{\sigma} - (\sigma_0 + R) \le 0$ defines the elastic domain of the material, where σ_0 is the reference yield stress. The effective stress $\bar{\sigma}$, based on Hershey's isotropic yield criterion with high exponent [24], is then defined in terms of the Cauchy stress tensor $\boldsymbol{\sigma}$ by

$$\bar{\sigma} = \bar{\sigma}(\boldsymbol{\sigma}) = \left[\frac{1}{2} \left\{ |\sigma_1 - \sigma_2|^m + |\sigma_2 - \sigma_3|^m + |\sigma_3 - \sigma_1|^m \right\} \right]^{\frac{1}{m}}, \tag{4}$$

where m is a material constant and $(\sigma_1, \sigma_2, \sigma_3)$ are the principal stresses. For shell elements, the yield criterion is defined in terms of the co-rotational stress tensor $\hat{\boldsymbol{\sigma}}$ (see Table 2), and a plane stress state is assumed. In this case, the effective stress reads

$$\bar{\sigma} = \bar{\sigma}(\hat{\boldsymbol{\sigma}}) = \left[\frac{1}{2} \left\{ |\hat{\sigma}_1|^m + |\hat{\sigma}_2|^m + |\hat{\sigma}_1 - \hat{\sigma}_2|^m \right\} \right]^{\frac{1}{m}}, \tag{5}$$

where $(\hat{\sigma}_1, \hat{\sigma}_2)$ are the principal stresses in the plane of the sheet. It is noted that for $m = 2$ the criterion coincides with the classical von Mises yield criterion. According to Logan and

Hosford [25], the isotropic yield locus for randomly oriented bcc materials is better approximated by the exponent m equals 6. In the present study, $m = 6$ was used even though a dual-phase material is considered.

Isotropic hardening is defined by a two-component Voce rule for small to moderate strains

$$R(\bar{\varepsilon}) = \sum_{i=1}^{2} Q_i (1 - \exp(-C_i \bar{\varepsilon})), \tag{6}$$

where $\bar{\varepsilon}$ is accumulated effective plastic strain, C_i and Q_i are material parameters determined from standard tensile tests. The rate form of Eq. (6) reads

$$\dot{R} = H_R \dot{\bar{\varepsilon}}, \quad H_R = \sum_{i=1}^{2} C_i Q_i \exp(-C_i \bar{\varepsilon}) \tag{7}$$

It is seen from Eq. (6) that the strain hardening saturates for large strains with a maximum value $R = \sum_{i=1}^{2} Q_i$. Saturation is not always confirmed by experiments, and nearly linear hardening has been reported for large strains [1, 26]. To account for this phenomenon, the strain hardening evolution rule is modified to read

$$\dot{R} = \max(H_R, H_{R,\min}) \dot{\bar{\varepsilon}}, \tag{8}$$

where $H_{R,\min}$ is the minimum work hardening rate. This quantity may be identified from experiments at large plastic strains, e.g. from the shear test. It follows that Eq. (6) is valid until an effective plastic strain $\bar{\varepsilon}^*$ only, which is implicitly defined by

$$H_{R,\min} = \sum_{i=1}^{2} C_i Q_i \exp(-C_i \bar{\varepsilon}^*) \tag{9}$$

It will be shown below that this option provides better results for problems involving large plastic deformations.

5.2 Failure criterion

To describe ductile failure of the material, the simple phenomenological criterion proposed by Cockcroft and Latham [21] was employed. In this failure criterion, the element is eroded when

$$W = \int_0^{\bar{\varepsilon}} \max(\sigma_1, 0) d\bar{\varepsilon} \geq W_C \tag{10}$$

where σ_1 is the maximum principal stress and W_C is the critical value of the integral W that should be determined from an appropriate experiment. In the model, the fracture criterion is coupled with the element erosion algorithm available in LS-DYNA. Element erosion occurs when $W \geq W_C$ in one or more integration points of an element, and this element is removed from the finite element model. Element removal may not be a generally applicable approach for describing material failure. However, in this work, attention is given to the onset of failure rather than crack propagation.

5.3 Identification of material parameters

The elastoplastic model contains several material parameters that have to be identified from suitable experiments. It is a common practice to identify the hardening parameters from simple uniaxial tensile tests. In this study, the parameters of the two-component Voce rule are determined from the uniaxial tension test, while the linear hardening for large strains and the fracture parameter are determined from the shear test.

5.3.1 Strain hardening

The results of uniaxial tensile tests up to diffuse necking were used to determine strain-hardening parameters in Eq. (6) namely σ_0, Q_i and C_i ($i = 1, 2$). These parameters were deduced by fitting Eq. (6) to the quasi-static Cauchy stress vs. logarithmic plastic strain curve in the rolling direction for specimen mts0002, which is chosen as the reference test. A least square method is applied for minimizing the error between experimental data and calculated results. Fig. 12a shows that the chosen strain hardening model describes the experimental behaviour well. The identified parameters are gathered in Table 3.

5.3.2 Minimum work hardening rate

The two-component Voce hardening rule, described by Eq. (6), and calibrated from uniaxial tensile tests converges asymptotically to a zero work hardening rate at relatively moderate strains. However, this behaviour is not in accordance with the data obtained from the shear tests, and thereby a minimum work hardening rate was introduced in addition to the above hardening parameters as described in Section 5.1. As seen in Fig. 12b, the model without the minimum work hardening rate parameter was not able to predict the experimental nominal shear stress vs. elongation behaviour at large displacements. Thus, the minimum work hardening rate $H_{R,\min}$ is determined for large plastic strains from the shear test by correlating experimental and numerical nominal shear stress-elongation curves through a trial-and-error procedure. In this context, numerical simulations are carried out with shell elements. Fracture was excluded by prescribing a large value of W_C. Further details about the numerical simulations are described in Section 6. It was found that reasonable predictions were obtained with $H_{R,\min}$ = 200 MPa for the investigated dual-phase steel, see Fig. 12b, and this value was used for subsequent simulations.

5.3.3 Ductile fracture

The Cockcroft-Latham fracture criterion has only one parameter, W_C, that presently is identified from the in-plane shear test. The parameter can not be identified directly from the measured force-elongation characteristics, since the stress and strain fields are inhomogeneous within the shear zone. Attempts to use analytical calculations resulted in severe underestimations of the fracture parameter [1, 26]. Therefore, an FE-based technique is adopted to identify the fracture parameter W_C. This technique relies on an acceptable correlation between the experimental and simulated force-elongation curve. When this is obtained, a simulation is carried out in which W_C is given a large value to exclude fracture. During the simulation, the integral W is continuously calculated. At an elongation corresponding to the maximum force in the experiment, the maximum value of W within the shear zone is determined from the simulation and taken as the fracture parameter W_C. The evolution of the integral W depends on the state of stress as well as on the strains developed. In order to assess the influence of stress triaxiality, numerical simulations with brick elements were performed and compared with the shell element simulations.

As can be seen from Fig. 13, satisfactory agreement is found between the experiments and simulations using shell and brick element models in terms of nominal shear stress-elongation characteristics. The maximum value of the fracture integral W within the shear zone is calculated through the numerical analysis and is plotted as a function of elongation in Fig. 13. The fracture parameter W_C is determined as the maximum value of W at an elongation corresponding to incipient fracture in the experiments. Accordingly, W_C is found to be in the order of 590 MPa based on the shell element simulation and around 610

MPa based on the simulation with brick elements. A detailed description of the FE models used in the simulations of the shear test is given in the subsequent section.

6 Numerical simulations

The explicit solver of the non-linear finite element code LS-DYNA [22] was used for the computational analyses of the in-plane shear test. The simulations were carried out using the material model presented in Section 5, and the corresponding model parameters are summarized in Table 3. In addition to the constitutive law given in Table 2, the material model also includes the Cockcroft-Latham failure criterion that allows elements to be removed from the mesh after a critical value is exceeded using the element erosion algorithm of LS-DYNA.

The FE shell model of the in-plane shear specimen was made using the mesh generator of the code I-DEAS [27]. The model is shown in Fig. 14 and consists of 4550 shell elements with selective reduced integration (LS-DYNA type 16). Two through thickness integration points were used. Effort was made to create a finer mesh in the concentrated shear zone, while a coarse mesh was made outside the gauge section. An element size of approximately 0.08 mm × 0.08 mm was used in the shear zone and found to be sufficient for representing the observed behaviour. The dimensions of the FE model are equal to those of the physical specimens with a shear zone of 2.5 mm. The clevis pins were modelled using rigid shell elements in order to be consistent with the experimental conditions. The right pin was fixed, while the left pin was given a displacement boundary condition through a smooth curve function in LS-DYNA.

The 3D model of the specimen was generated using the shell drag option in LS-PREPOST on the basis of a shell model. Since the shear specimen is symmetric in the thickness direction, one half of the specimen was modelled by taking into account the thickness symmetry boundary condition, resulting in a total of 17295 elements with 5 elements in the thickness direction. The analyses were performed using eight-node brick elements with on-point integration. The approximate element size used in the shear zone was 0.07 mm × 0.09 mm × 0.15 mm.

Numerical predictions of damage and fracture are prone to mesh dependent. In plane stress formulations (i.e. for shell elements), predictions of localized necking due to plastic thinning are also sensitive to the mesh density. Non-local plastic thinning was proposed by Wang et al. [20] to improve the convergence characteristics of such simulations. In this approach, the average plastic thickness strain rate within a radius of influence surrounding the integration point is calculated and used to predict the thinning of the shell. In the model implementation, the following non-local equations are considered for the shell elements. Assume that the non-local value of the plastic strain rate in the thickness direction $\dot{\varepsilon}_{33}^{p}(\mathbf{x}_r)$ is to be calculated for an integration point with position vector $\mathbf{x}_r \in \Omega_r$ in a given shell layer. Let Ω_r denote the neighbourhood within a given radius L of this integration point included in the same layer of the shell element. The non-local plastic strain rate [28] is defined by

$$\dot{\varepsilon}_{33}^{p}(\mathbf{x}_r) = \frac{1}{W(\mathbf{x}_r)} \int_{\Omega_r} \dot{\varepsilon}_{33}^{p}(\mathbf{y}) w(\mathbf{x}_r - \mathbf{y}) d\Omega \tag{11}$$

where

$$w(\mathbf{x}_r - \mathbf{y}) = \frac{1}{\left[1 + \left(\frac{|\mathbf{x}_r - \mathbf{y}|}{L}\right)^p\right]^q}; \quad W(\mathbf{x}_r) = \int_{\Omega_r} w(\mathbf{x}_r - \mathbf{y}) d\Omega \tag{12}$$

In the above equations, $\dot{\varepsilon}_{33}^p(\mathbf{y})$ is the local plastic strain rate of the integration point, $\mathbf{y}$ is the local position vector within the domain Ω_r, w is a weight function, and the parameters p and q are user-defined exponents of the weight function. Further details regarding non-local thinning are provided by Wang et al. [20]. In the present study, the radius of the non-local domain L for the shear test is taken as approximately half of the sheet thickness, i.e. 0.70 mm. The parameters p and q are set to zero, i.e. equal weight is given to the integration points within the non-local domain.

7 Comparison and discussion

Experimental results in terms of mode of deformation, nominal shear stress-elongation characteristics, strain contours and various strain measures (shear angle, stretch ratios and logarithmic thickness strain) versus elongation, are compared with the numerical predictions in this section.

The nominal shear stress-elongation curves from experiments and simulations with shell and brick elements after including the failure parameter are depicted in Fig. 15a. A fairly good correlation between the experimental and numerical nominal shear stress-elongation curves is observed. From Fig. 13 it is seen that a 3 % higher estimate of the fracture parameter W_C was found in brick element simulations. Accordingly, there is some

influence of the three-dimensional stress state on the evolution of the integral W in the shear test. In general, W increases more rapidly under higher stress triaxiality level, and a higher estimate of W_C should be expected from the brick element analyses. However, this result indicates that the stress triaxiality stays at a low level even for large strains in the shear test. Fig. 15b depicts plots of effective plastic strain $\bar{\varepsilon}$ vs. stress triaxiality $\frac{\sigma_m}{\bar{\sigma}}$, where σ_m is the mean stress and $\bar{\sigma}$ is the effective stress, for two critical elements in the shell and brick element models. As seen from Fig. 15b, higher stress triaxiality values are apparent in the brick element model, which is in accordance with the 3 % higher estimate of W_C. At incipient failure, the stress triaxiality is about 0.16 in the shell model and 0.23 in the brick model. These values are considered to be in the low stress triaxiality regime, according to Bao and Wierzbicki [9].

As the global response is well predicted, it is interesting to compare the local strain measurements from the experiments with the strains calculated in the simulations. Fig. 16 compares the Green-Lagrange shear strain E_{xy} in the shear zone, measured by digital image correlation and computed using shell elements. It should be noted that all the contours in the figure are displayed with a fixed scale. The shear deformation in both cases is concentrated in the gauge area and very small deformations are observed in the rest of the specimen. The numerical simulation reproduces the deformation mode seen in the experiment, which is a necessary requirement for the application of the FE-based technique used to identify the fracture parameter. However, the estimated Green-Lagrange shear strain at the onset of fracture in the numerical simulation is approximately 85 %, whereas it

is in the order of 70 % in the experiment. Some of the difference might be attributed to the possible difference in sizes of the element used in the experiments and simulations. The element size in the experiments is approximately 0.2 mm × 0.2 mm, whereas the element size in simulations is in the order of 0.08 mm × 0.08 mm. As the element size used in the digital image correlation is larger than that used in the FE simulations, it may not capture very accurately strain gradients, and therefore the maximum level is smaller in the experiment. Fig. 17 shows the stretch ratios λ_1 and λ_2 in the rolling (loading) and transverse directions, the shear angle γ, and the logarithmic thickness strain ε_{33} calculated from field measurements and FE simulations. The values are taken for a single element in the centre of the gauge area. As can be seen from Fig. 17a, the stretch ratio λ_1 in the loading direction is somewhat over-predicted in the FE simulations, while the predicted stretch ratio λ_2 in the transverse direction is comparable to that of the experiment, see Fig. 17b. The shear angle is larger in the numerical simulations than in the experiments, Fig. 17c, and this is in agreement with the results presented in Fig. 16. Fig. 17d shows the logarithmic thickness strain ε_{33} against elongation. There is some difference in the thinning between simulations and experiments, which could be attributed to the deviations found in the in-plane deformations. However, it is recalled that significant scatter in the thickness strain was found between duplicate tests.

The large differences in effective plastic strain to failure in the shear test (of the order of 1.0) compared with the conventional uniaxial tensile tests (of the order of 0.15 up to maximum load, see Fig. 8a) is noteworthy. The shear test thus provides information on the material behaviour for significantly larger strains and for different states of stress than in

the uniaxial tensile tests, and therefore has a potential for use in calibration and validation of constitutive laws and fracture criteria [1, 26].

Fractured specimens from experiments and simulations are illustrated in Fig. 18. Fracture occurs in the core of the shear zone as a result of combined shear and tensile stresses. The simulations predict the onset of fracture within the localised shear zone. However, the crack in the simulations looks somewhat serrated because of the element erosion algorithm, whereas the crack in the experiments appears smooth. The validation of the Cockcroft-Latham fracture criterion is beyond the scope of the present paper. The aim was to illustrate how the shear test in combination with field measurements could be used to identify a given fracture criterion. However, it should be noted that the Cockcroft-Latham fracture criterion has been validated for different materials and used in various applications with good results [29-32].

Additional analyses using $m = 2$ were carried out to study the influence of the yield criterion exponent, which determines the shape of the yield surface. It is seen from Fig. 19 that for both shell and brick models, the values of $m = 2$ and $m = 6$ resulted in almost the same behaviour. In particular, the initial elastic to plastic transition region is very well predicted with $m = 6$, whilst the behaviour after the transition region is better predicted with $m = 2$. Moreover, only one stress path (shear) is considered in the present investigation, which eventually provided a response of the same accuracy for both $m = 2$ and 6 using shell and brick elements.

8 Concluding remarks

The stress-strain behaviour and plastic anisotropy of a dual-phase high-strength steel DP800 sheet was investigated by means of uniaxial tension tests in various directions with respect to the rolling direction. Only weak plastic anisotropy was detected. Monotonic, quasi-static in-plane shear tests were carried out to assess the work hardening behaviour at large plastic strain and ductile fracture. A full-field measuring system based on digital image correlation was applied to evaluate the displacements and strains in the gauge area up to fracture. It is worth noticing that the in-plane shear test provides substantial information concerning the material behaviour at large strains and for different states of stress than the uniaxial tensile test. Furthermore, the in-plane shear tests also give information about ductile failure with presumably minor effects of plastic instability. Thus, the information gained from the shear tests can be used in calibration and/or validation of constitutive relations and fracture criteria.

The experimental behaviour was modelled using LS-DYNA and an elastoplastic constitutive model with high-exponent isotropic yield criterion. It was shown that the constitutive model predicted the experimental results in terms of load-elongation characteristics and mode of deformation with good accuracy. Consistent results were obtained with shell and brick elements. The local strains obtained in the numerical simulations were in reasonable agreement with the experimental observations by digital image correlation. In addition, it was shown how a fracture criterion, in this case the Cockcroft-Latham criterion, could be identified from the shear test by an FE-based

technique. The calibrated fracture criterion was then used to model ductile failure in shell and brick element simulations.

Acknowledgement

The present work has been carried out with financial support from the Research Council of Norway through the strategic university programme "Design of Crashworthy Light Structures" and support from the Norwegian University of Science and Technology. Thankful acknowledgement is also made to SSAB for supplying the test material.

References

[1] Lademo OG, Eriksson M, Reyes A, Hopperstad OS, Langseth M (2006) Characterisation of failure and identification of failure related parameters. SINTEF report STF80MK F06083, Trondheim (Norway).

[2] Rauch EF (1998) Plastic anisotropy of sheets determined by simple shear tests. Mater Sci Eng A 241:179-183.

[3] Bouvier S, Haddadi H, Levee P, Teodosiu, C (2006) Simple shear tests: Experimental techniques and characterization of the plastic anisotropy of rolled sheets at large strains. J Mater Proc Technol 172:96-103.

[4] Bouvier S, Gardey B, Haddadi H, Teodosiu C (2006) Characterization of the strain-induced plastic anisotropy of rolled sheets by using sequences of simple shear and uniaxial tensile tests. J Mater Proc Technol 174:115-126.

[5] Rauch EF, G'Sell C (1989) Flow localization induced by a change in strain path in mild steel. Mater Sci Eng A 111:71-80.

[6] Rauch EF, Schmitt JH (1989) Dislocation substructures in mild steel deformed in simple shear. Mater Sci Eng A 113:441-448.

[7] Iosipescu N (1967) New accurate procedure for single shear testing of metals. J Mater 2:537-566.

[8] Barnes JA, Kumosa M, Hull D (1987) Theoretical and experimental evaluation of the Iosipescu shear test. Compos Sci Technol 28:251-268.

[9] Bao Y, Wierzbicki T (2004) On fracture locus in the equivalent strain and stress triaxiality space. Int J Mech Sci 46(1):81-98.

[10] Burr A, Hild F, Leckie FA (1997) Continuum description of damage in ceramic-matrix composites. Eur J Mech A/Solids 16(1):53-78.

[11] Bruck HA, McNeill SR, Sutton MA, Peters WH (1989) Digital image correlation using Newton-Raphson method for partial differential correction. Exp Mech 29:261-267.

[12] Sutton MA, McNeill SR, Helm JD, Chao YJ (2000). Advances in two-dimensional and three-dimensional computer vision. In: Rastogi PK(ed.) Photomechanics. Springer, Berlin (Germany) pp 323-372.

[13] Hild F, Raka B, Baudequin M, Roux S, Cantelauble F (2002) Multiscale displacement field measurements of compressed mineral-wool samples by digital image correlation. Appl Optics 41(32):6815-6828.

[14] Chu TC, Ranson WF, Sutton MA, Peters WH (1985) Applications of digital-image-correlation techniques to experimental mechanics. Exp Mech 25:232-244.

[15] Besnard G, Hild F, Roux S (2006) "Finite-Element" displacement fields analysis from digital images: Application to Portevin-Le-Châtelier bands. Exp Mech 46:789-803.

[16] Tay CJ, Quan C, Huang YH, Fu Y (2005) Digital image correlation for whole field out-of-plane displacement measurement using a single camera. Opt Commun 251:23-36.

[17] Khan AS, Huang S (1995) Continuum theory of plasticity. John Wiley & Sons, Inc, New York.

[18] Bergonnier S, Hild F, Roux S (2005) Strain heterogeneties in tension and compression tests on mineral wool samples. J Strain Analysis 40(2):185-197.

[19] Reyes A, Hopperstad OS, Lademo OG, Langseth M (2006) Modelling of textured aluminum alloys used in a bumper system: Material tests and characterization. Comp Mater Sci 37(3): 246-268.

[20] Wang T, Hopperstad OS, Lademo OG, Larsen PK (2006) Finite element analysis of welded beam-to-column joints in aluminium alloy EN AW 6082 T6. Submitted for publication.

[21] Cockcroft MG, Latham DJ (1968) Ductility and the workability of metals. J Inst Met 96:33-39.

[22] Hallquist JO (1998) LS-Dyna Theoretical Manual. Livermore Software Technology Corporation.

[23] Berstad T, Lademo OG, Hopperstad OS (2005) Weak and strong texture models in LS-DYNA (WTM-2D/3D and STM-2D). SINTEF report STF80MK F05180.

[24] Hershey AV (1954) Plasticity of isotropic aggregate of anisotropic facecentred cubic crystals. J Appl Mech 21(3): 241-249.

[25] Logan RW, Hosford WF (1980) Upper bound anisotropic yield locus calculations assuming $\langle 111 \rangle$- pencil glide. Int J Mech Sci 22(7):419-430.

[26] Eriksson M, Lademo OG, Hopperstad OS (2006) Development and use of in-plane shear tests to identify ductile failure parameters of aluminium alloys. Proceedings of 9th international conference on material forming (ESAFORM-2006), Glasgow, April 26-28, pp. 331-334.

[27] SDRC (1993) I-DEAS Master series, Exploring I-DEAS Design.

[28] Worswick MJ, Pilkey AK, Lalbin X, Truttmann S, Liu G, Fowler J (2000) Prediction of ductile fracture under high strain rate conditions. Final report for SNC Industrial Technologies, Defence Research Establishment Valcartier (DREV), Defence Research Establishment Suffield (DRES).

[29] Dey S, Børvik T, Hopperstad OS, Langseth M (2006) On the influence of fracture criterion in projectile impact of steel plates. Comp Mater Sci (38):176-191.

[30] Dørum C, Hopperstad OS, Lademo OG, Langseth M (2005) Numerical modelling of the structural behaviour of thin-walled cast magnesium components. Int J Solids Struct 42: 2129-2144.

[31] Kwak TS, Kim YJ, Bae WB (2002) Finite element analysis on the effect of die clearance on shear planes in fine blanking. J Mater Process Technol 130-131: 462-468.

[32] Ko DC, Kim BM, Choi, JC (1996) Prediction of surface-fracture initiation in the axisymmetric extrusion and simple upsetting of an aluminum alloy. J Mater Process Technol 62 (1-3): 166-174.

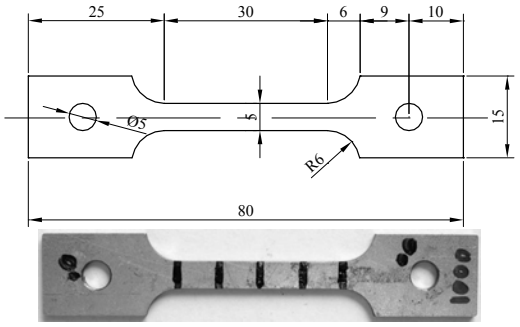

Fig. 1. Geometry of the uniaxial tensile test specimen

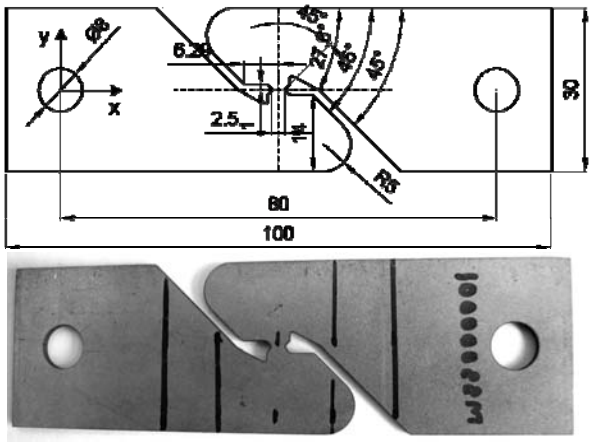

Fig. 2. Geometry of the in-plane shear test specimen

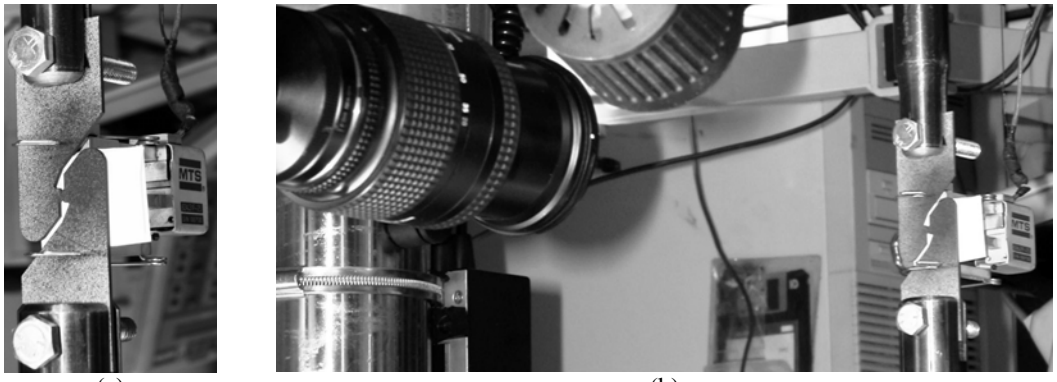

(a) (b)

Fig. 3. Experimental set-up for in-plane shear tests, (a) specimen with extensometer, and (b) specimen and camera

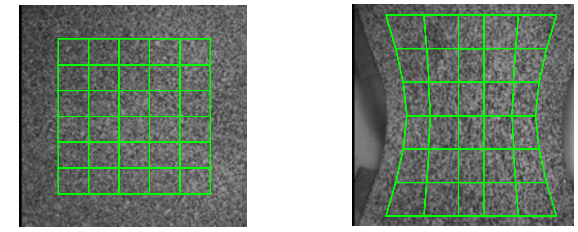

Fig. 4. Schematic representation of FE-based DIC

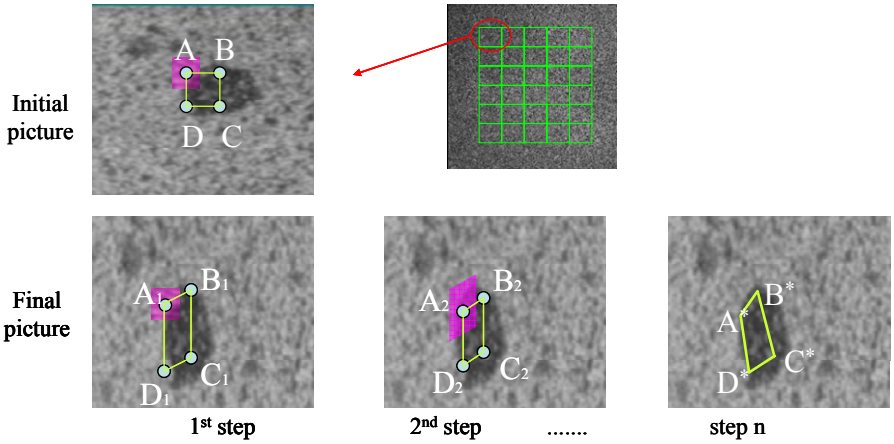

Fig. 5. Field determination principle of DIC

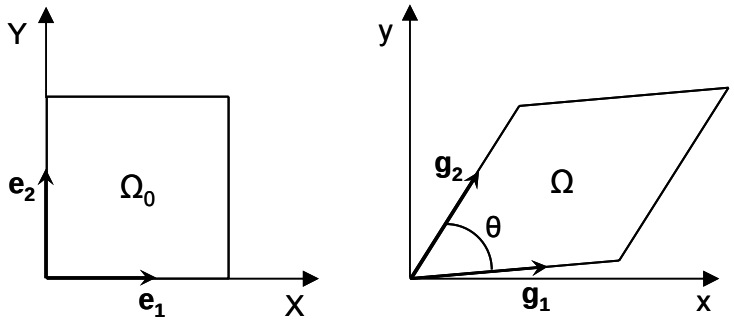

Fig. 6. Shear deformation represented by the angle between two adjacent, orthogonal fibers in the initial Ω_0 and current Ω configurations

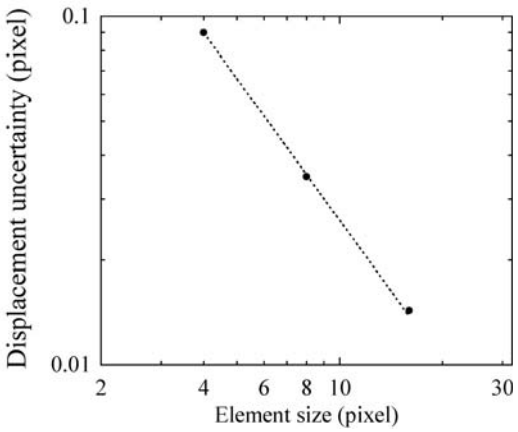

Fig. 7. Displacement uncertainty as a function of ZOI size for quasi-static in-plane shear test, mss02

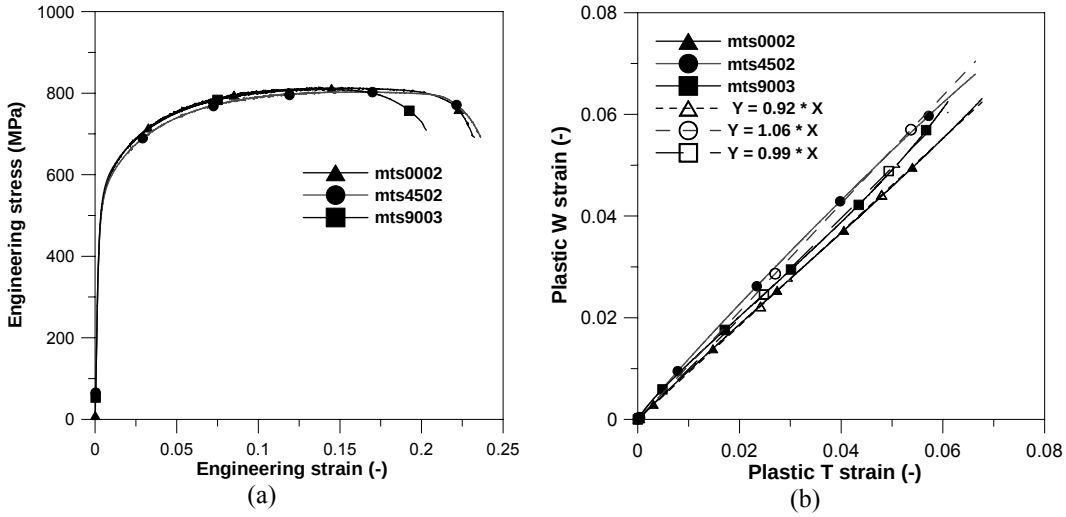

Fig. 8. Quasi-static tensile test results for one representative test in each direction of DP800, (a) engineering stress-strain curves, and (b) plots for determination of R-value

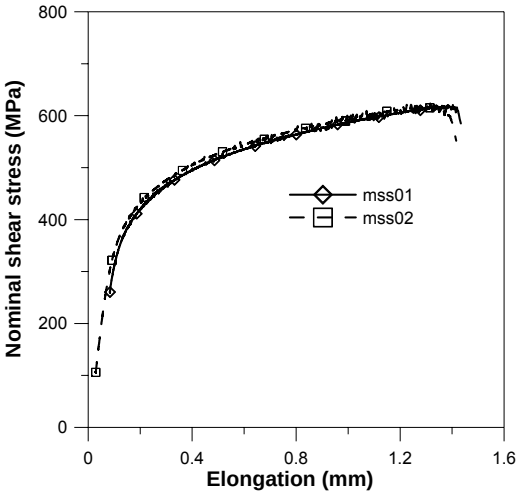

Fig. 9. Nominal shear stress vs. extensometer elongation for the quasi-static in-plane shear tests

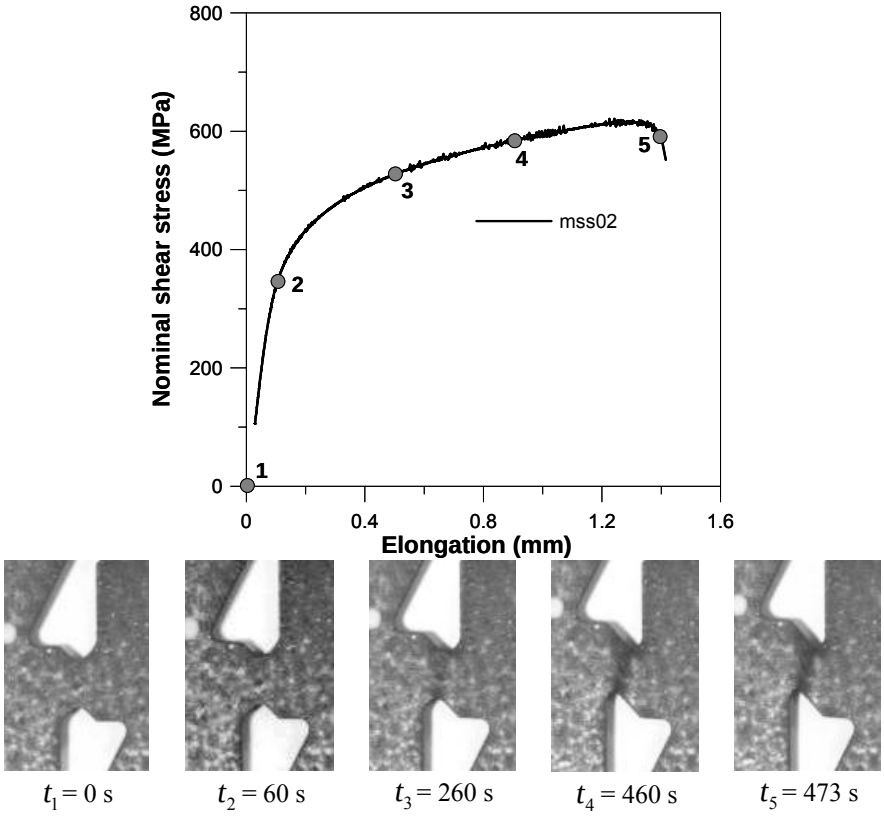

Fig. 10. Sequence of digital images for a quasi-static in-plane shear test, mss02

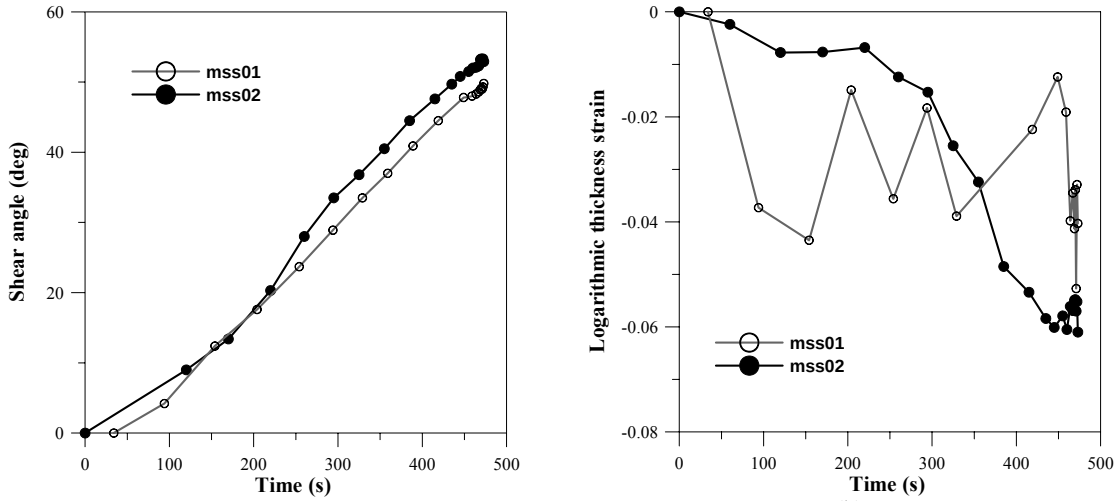

(a) (b)

Fig. 11 (a) Shear angle vs. time, and (b) logarithmic thickness strain vs. time, evaluated from the estimated displacement field for the two duplicate shear tests

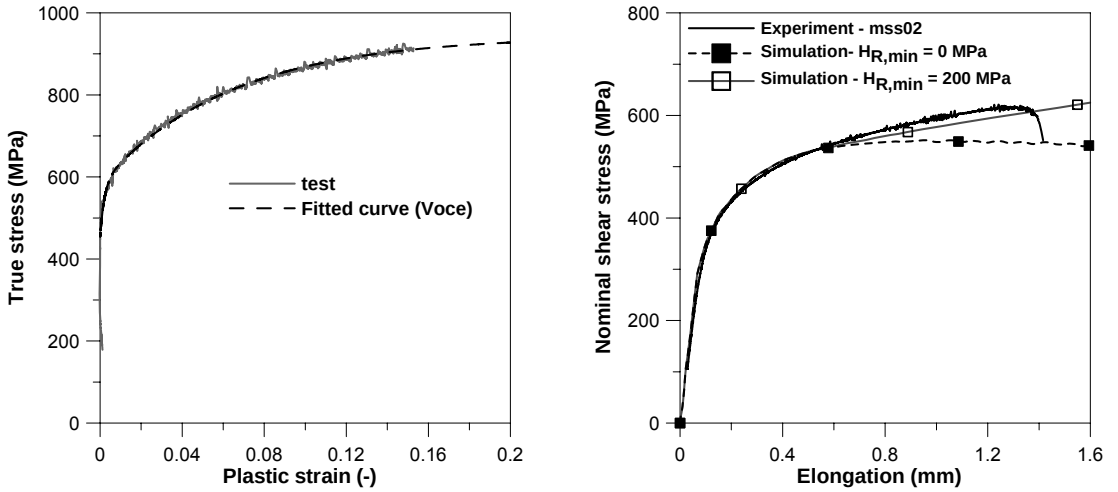

a) Strain-hardening, tensile test b) Minimum work hardening rate, shear test

Fig. 12 (a) Experimental and fitted strain-hardening curves and (b) nominal shear stress vs. elongation curves for the in-plane experimental shear tests compared with simulations with different values of the minimum work hardening rate, $H_{R,\min}$

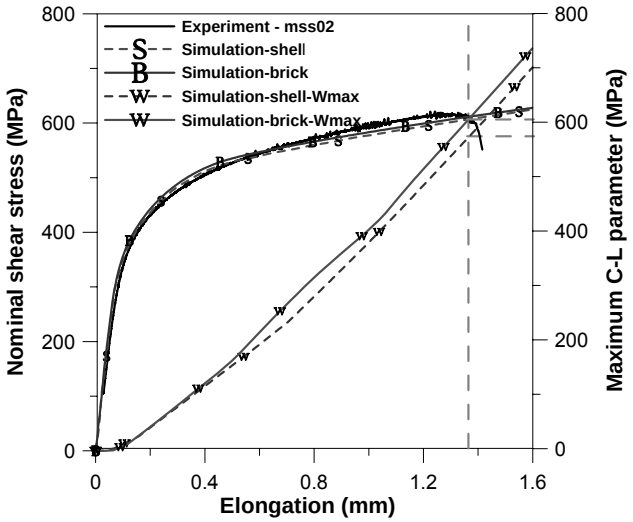

Fig. 13. Correlation of nominal shear stress-elongation curves from experiments and simulations (both shell & brick elements) including plots of $W_{\max}$, for in-plane shear test

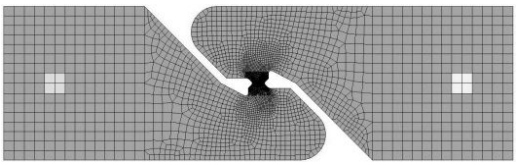

Fig. 14. FE model of the in-plane shear specimen

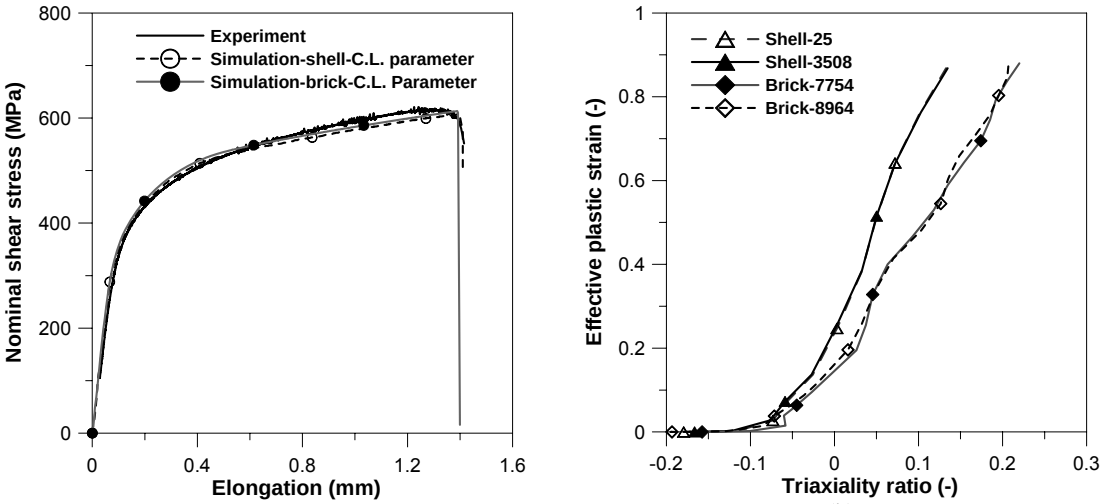

Fig. 15 (a) Experimental and numerical nominal shear stress vs. elongation curves after including failure parameter, and (b) comparison of plastic strain ($\bar{\varepsilon}$) vs. stress triaxiality ($\sigma_m/\bar{\sigma}$) between shell and brick element simulations of shear test

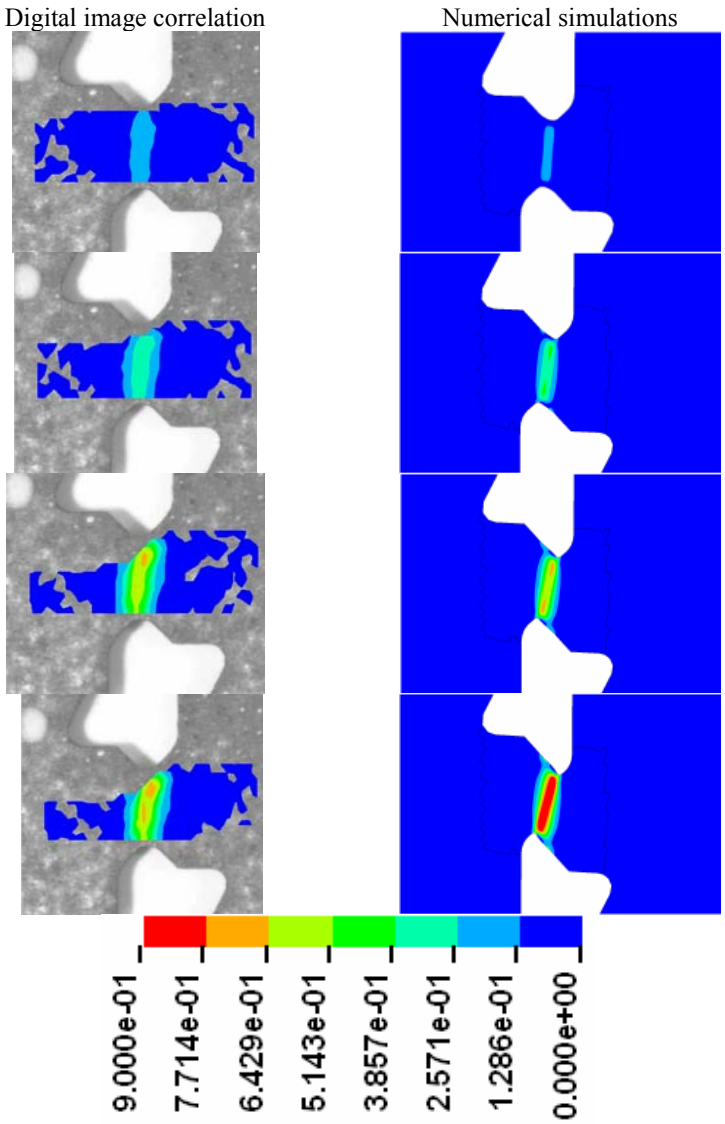

Fig. 16. Comparison of Green-Lagrange shear strain (E_{xy}) plots at different deformation stages between digital image correlation (for mss02) and numerical simulations representing with the same colour scale

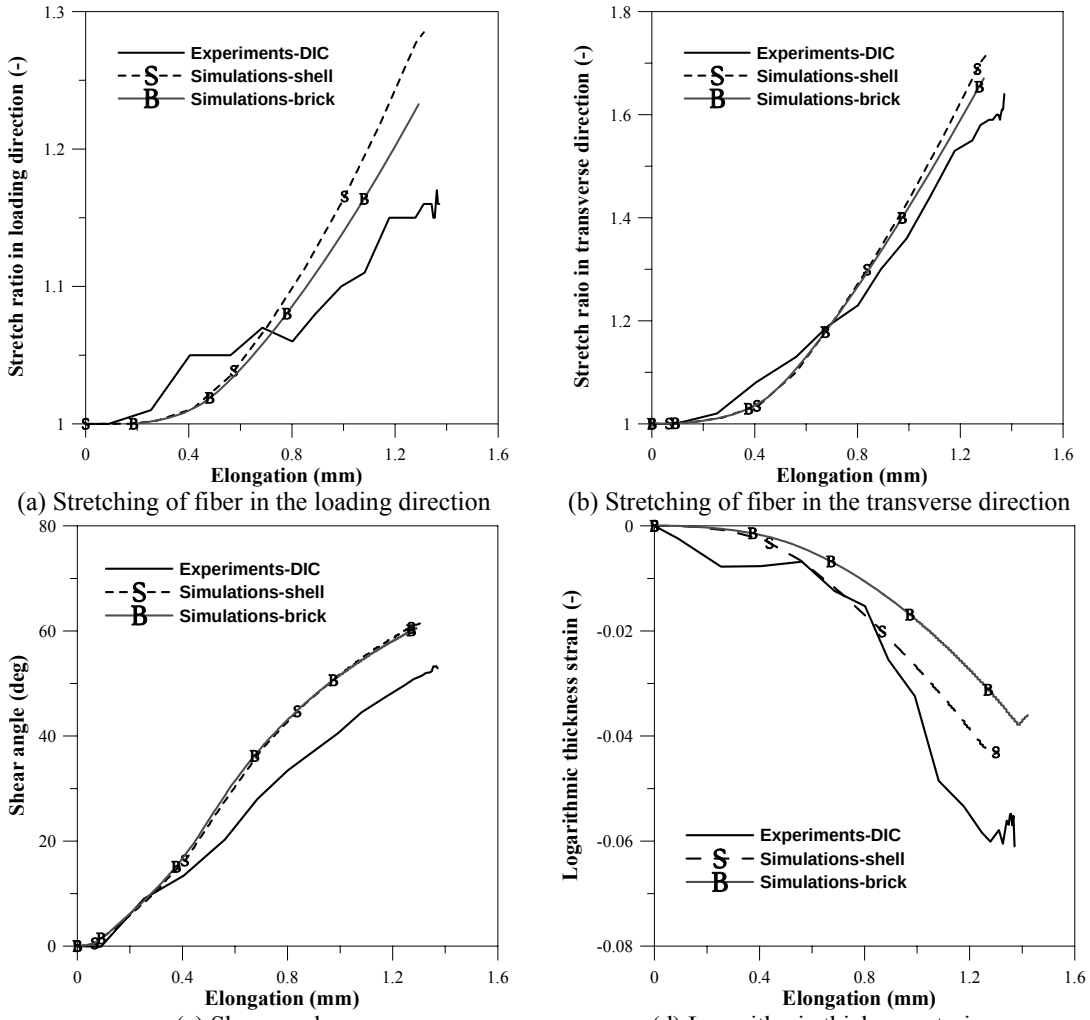

(a) Stretching of fiber in the loading direction

(b) Stretching of fiber in the transverse direction

(c) Shear angle

(d) Logarithmic thickness strains

Fig. 17 Comparison of local measurements against elongation between experiments and simulations with shell and brick element models

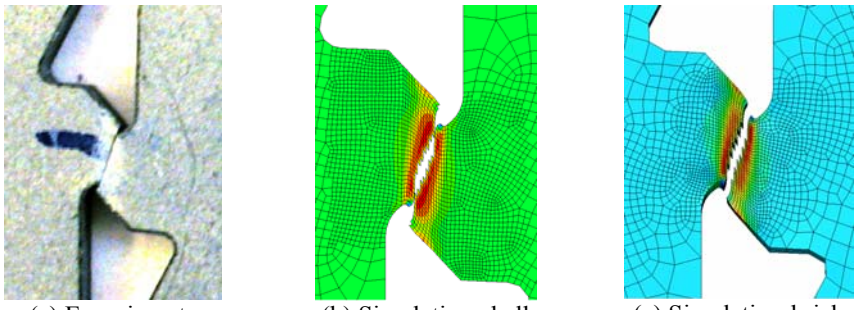

(a) Experiments

(b) Simulation-shell

(c) Simulation-brick

Fig. 18. Comparison of fractured shear zone from experiments, mss02, and simulations

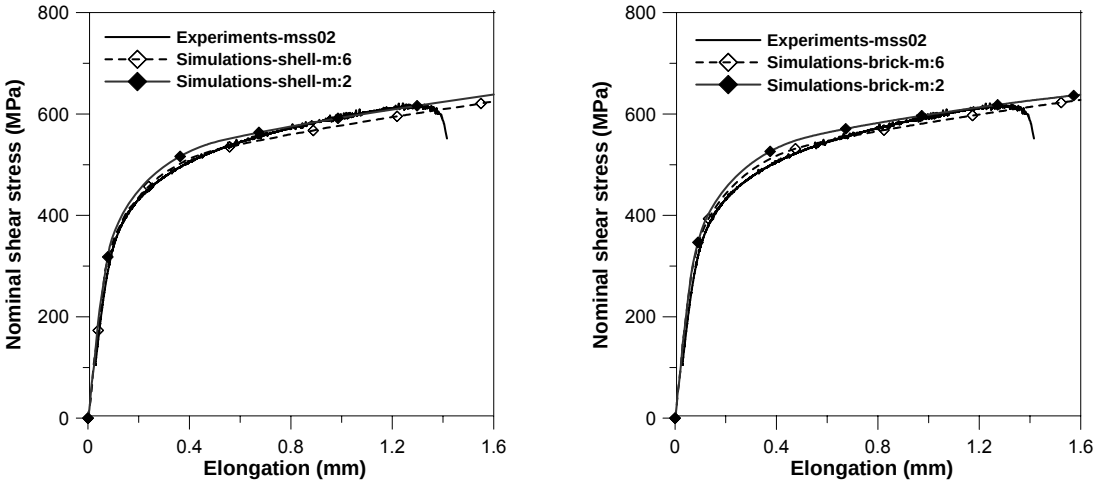

Fig. 19. Influence of exponent (m) in the yield criterion on the predicted nominal shear stress-deformation behaviour in (a) shell element model, and (b) brick element model

Table 1. Material characteristics for DP800

	Width w [mm]	Thickness t [mm]	Yield stress $s_{0.2}$ [MPa]	Maximum stress s_u [MPa]	Plastic strain ratio R [-]
mts0001	5.02	1.490	543	812	0.86
mts0002	5.09	1.496	529	815	0.92
mts0003	5.04	1.492	545	816	0.84
mts4501	5.01	1.487	532	809	0.99
mts4502	5.02	1.504	526	804	1.06
mts4503	5.04	1.498	525	793	1.01
mts9001	5.01	1.500	539	803	0.97
mts9002	5.04	1.493	544	811	1.04
mts9003	5.06	1.488	542	811	0.99

Table 2. Basic constitutive equations for shell (co-rotational) and brick elements

Shell element formulation (co-rotational)	Brick element formulation (Jaumann)
Additive decomposition of rate-of-deformation tensor into elastic and plastic parts	
$\hat{\mathbf{D}} = \hat{\mathbf{D}}^e + \hat{\mathbf{D}}^p, \quad \hat{\mathbf{D}} = \mathbf{R}^T \cdot \mathbf{D} \cdot \mathbf{R}$	$\mathbf{D} = \mathbf{D}^e + \mathbf{D}^p$
Hypoelastic stress-strain relation on rate form	
$\dot{\hat{\boldsymbol{\sigma}}} = \mathbf{C} : \hat{\mathbf{D}}^e, \quad \hat{\boldsymbol{\sigma}} = \mathbf{R}^T \cdot \boldsymbol{\sigma} \cdot \mathbf{R}$	$\boldsymbol{\sigma}^{\nabla J} = \mathbf{C} : \mathbf{D}^e$
Yield criterion	
$f(\hat{\boldsymbol{\sigma}}, R) = \bar{\sigma}(\hat{\boldsymbol{\sigma}}) - (\sigma_0 + R) \le 0$	$f(\boldsymbol{\sigma}, R) = \bar{\sigma}(\boldsymbol{\sigma}) - (\sigma_0 + R) \le 0$
Associated flow rule	
$\hat{\mathbf{D}}^p = \dot{\lambda} \frac{\partial f}{\partial \hat{\boldsymbol{\sigma}}}, \quad \dot{\bar{\varepsilon}} = -\dot{\lambda} \frac{\partial f}{\partial R} = \dot{\lambda}$	$\mathbf{D}^p = \dot{\lambda} \frac{\partial f}{\partial \boldsymbol{\sigma}}, \quad \dot{\bar{\varepsilon}} = -\dot{\lambda} \frac{\partial f}{\partial R} = \dot{\lambda}$
Loading/unloading conditions	
$f(\hat{\boldsymbol{\sigma}}) \le 0; \ \dot{\lambda} \ge 0; \ f\dot{\lambda} = 0$	$f(\boldsymbol{\sigma}) \le 0; \ \dot{\lambda} \ge 0; \ f\dot{\lambda} = 0$

Table 3. Identified parameters from the experiments for DP800

E [MPa]	ν [-]	σ_0 [MPa]	Q_1 [MPa]	C_1 [-]	Q_2 [MPa]	C_2 [-]	$H_{R,\min}$ [MPa]	m [-]
205000	0.3	420	178	337	388	15	200	6